

Oxygen, neon, and iron X-ray absorption in the local interstellar medium

Efraín Gattuzz^{1,2,3}, Javier A. García⁴, Timothy R. Kallman⁵, and Claudio Mendoza³

¹ Max-Planck-Institut für Astrophysik, 85741 Garching bei München, Germany e-mail: egattuzz@mpa-garching.mpg.de

² Escuela de Física, Facultad de Ciencias, Universidad Central de Venezuela, PO Box 20632, Caracas 1020A, Venezuela

³ Centro de Física, Instituto Venezolano de Investigaciones Científicas (IVIC), PO Box 20632, Caracas 1020A, Venezuela e-mail: claudio@ivic.gob.ve

⁴ Harvard-Smithsonian Center for Astrophysics, Cambridge, MA, 02138, USA e-mail: javier@head.cfa.harvard.edu

⁵ NASA Goddard Space Flight Center, Greenbelt, MD 20771, USA e-mail: timothy.r.kallman@nasa.gov

November 1, 2021

ABSTRACT

Aims. We present a detailed study of X-ray absorption in the local interstellar medium by analyzing the X-ray spectra of 24 Galactic sources obtained with the *Chandra* High Energy Transmission Grating Spectrometer and the *XMM-Newton* Reflection Grating Spectrometer.

Methods. By modeling the continuum with a simple broken power law and by implementing the new ISMabs X-ray absorption model, we estimated the total H, O, Ne, and Fe column densities toward the observed sources.

Results. We have determined the absorbing material distribution as a function of source distance and galactic latitude–longitude.

Conclusions. Direct estimates of the fractions of neutrally, singly, and doubly ionized species of O, Ne, and Fe reveal the dominance of the cold component, thus indicating an overall low degree of ionization. Our results are expected to be sensitive to the model used to describe the continuum in all sources.

Key words. ISM: general – ISM: atoms – ISM: abundances – ISM: structure – X-rays: ISM

1. Introduction

The interstellar medium (ISM) is one of the most important galactic components. Regarding its chemical composition, it can be enriched with heavy elements by gas accretion from other galaxies, supernova explosions, and stellar winds (Pinto et al. 2013). The analysis of such a dynamic environment is crucial for understanding stellar formation and evolutionary processes, which may be performed by means of high-resolution X-ray spectroscopy. Owing to their high penetrating power, X-ray photons interact not only with the ISM atomic ions exciting inner-shell levels but also with molecules and solid compounds, thus providing the opportunity to study physical properties, such as column densities, ionization fractions, and abundances of astrophysically relevant elements in both the gas and grains (Gattuzz et al. 2015).

Multiple ISM analyses using low-mass X-ray binaries (LMXB) have been carried out in the past decade that report the presence of a multiphase ISM structure, which includes a cold gas with low-ionization degree and a hot ionized gas (e.g., Schulz et al. 2002; Takei et al. 2002; Juett et al. 2004; Yao et al. 2009; Liao et al. 2013; Pinto et al. 2013); however, the identification of the highly ionized species is less straightforward than the lowly ionized ones. For example, Gattuzz et al. (2014) performed a study of eight LMXB using high-resolution *Chandra* spectra, detecting only a $K\alpha$ absorption feature (22.024 ± 0.003 Å) from highly ionized O VI toward XTE J1817-330. This line was previously identified by Gattuzz et al. (2013a,b) as being intrinsic to the source rather than originating in the local ISM. They concluded that the cold phase is dominant without any further iden-

tification of an associated hot gas component. In support of this view, Luo & Fang (2014) have found that most of the absorption lines from highly ionized metals detected in the spectra toward 12 LMXB arise in the hot gas intrinsic to the sources, the ISM only making a small contribution. In a recent study, Nicastro (2014) has concluded that the absorption line at ~ 22.275 Å is ubiquitously detected in the spectra of both Galactic and extragalactic sources. It leads to identifying O II $K\beta$ from the local ISM, thus contradicting its previous identification as an O VI $K\alpha$ absorption feature of the warm-hot intergalactic medium (WHIM) along the lines of sight toward H 2356–309 (Buote et al. 2009; Fang et al. 2010) and Mkn 501 (Ren et al. 2014).

Gattuzz et al. (2013a,b) made a detailed evaluation of the oxygen absorption region using *Chandra* high-resolution spectra from the bright binary XTE J1817–330, observing a complex structure around the K edge that included the presence of $K\alpha$, $K\beta$, and $K\gamma$ absorption lines from O I and O II and $K\alpha$ from O III, O VI, and O VII. Gattuzz et al. (2014) fit the O K edge in the *Chandra* spectra of eight LMXB with the warmabs photoionization model to determine the ISM ionization degree. In the same work, the O-photoabsorption cross-section computed by García et al. (2005) was compared with the most recent calculation by Gorczyca et al. (2013), finding no substantial differences in the modeling of the K-shell region. It is worth emphasizing the remarkable accuracy of the oxygen atomic data that was thereby established. The dominance of a neutral gas in all the observed lines of sight was therefore concluded in this work with ionic fractions O II/O I and O III/O I lower than 0.1.

In addition to oxygen, a benchmark of the neon atomic data was also pursued by Gattuzz et al. (2015). Using the high signal-

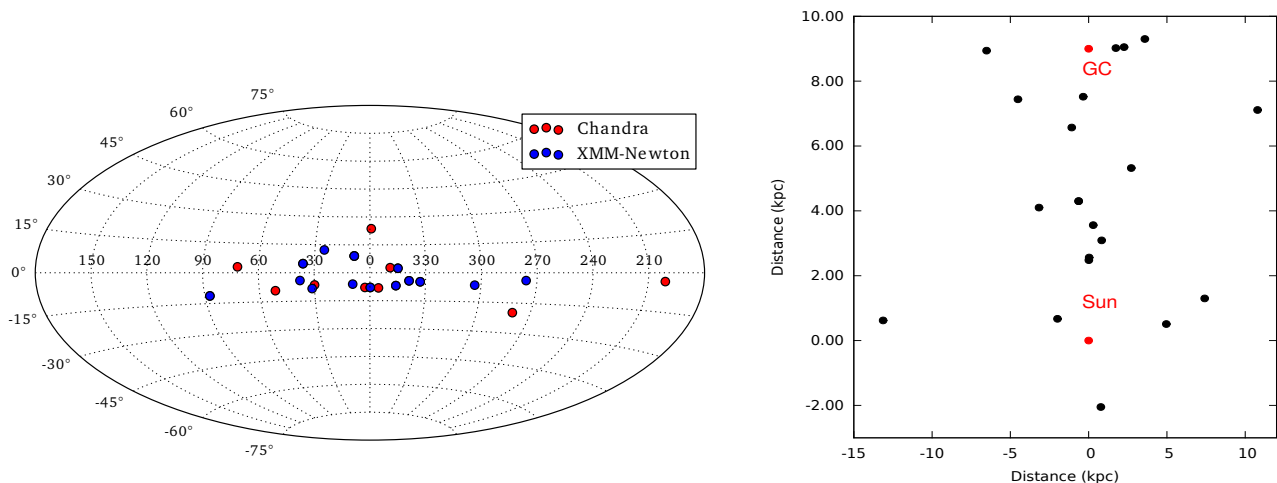


Fig. 1. Location map of the X-ray binaries of the present sample. The left panel shows the sources plotted on a full-sky map in galactic coordinates relative to the Galactic center. Red points: *Chandra* sources. Blue points: *XMM-Newton* sources. The right panel shows a location map of the X-ray binaries in our sample projected in the Galactic plane.

to-noise spectra of Cygnus X–2 and XTE J1817–330, the positions of the $K\beta$ absorption line in Ne I and $K\alpha$, $K\beta$, and $K\gamma$ in Ne II and Ne III were determined. The Ne I cross-section computed by Gorczyca & McLaughlin (2000) and those for Ne II and Ne III by Juett et al. (2006) were adjusted by shifting the wavelength scale in order to fit the astronomical spectra. With the improved cross sections, a new X-ray absorption model, referred to as ISMabs, was developed and made publicly available (Gatuzz et al. 2015). Its advantage lies in the compilation of a database of photoabsorption cross sections for neutrally, singly, and doubly ionized species for all the cosmic abundant elements, namely H, He, C, N, O, Ne, Mg, Si, S, Ar, Ca, and Fe. Although the neutral component is dominant in the ISM, it is found that including singly and doubly ionized species leads to more realistic models of the O and Ne K edges; furthermore, the use of a physical model prevents misidentification of absorption features that often occurs in the traditional fitting methods with Gaussian profiles.

ISM X-ray absorption affects all the X-ray observations and is particularly evident in high-resolution grating spectra. Even though a careful modeling of the ISM was previously attempted, its chemical composition and spatial distribution are still being debated (e.g., identification of a Galactic highly ionized gas and the existence of a homogeneous distribution on large scales). Moreover, an imprecise ISM modeling can lead to erroneous conclusions when analyzing other environments, such as the Galactic halo or the WHIM. In this respect, a comprehensive analysis of the ISM through multiple lines of sight and use of a realistic absorption model like ISMabs would be invaluable for addressing these concerns; consequently, we present an extensive analysis of the ISM using *XMM-Newton* and *Chandra* high-resolution X-ray spectra.

The outline of this report is as follows. In Section 2 the data reduction process is summarized, and in Section 3 the data-fitting procedure is described. A thorough discussion of the results is given in Section 4, and finally in Section 5, we draw the conclusions of this work.

2. Observations and data reduction

To carry out the present ISM study we have gathered a sample of X-ray binary spectra from the *XMM-Newton* Science Archive (XSA¹) and the *Chandra* Source Catalog (CSC²). A total of 24 bright sources were analyzed, 15 from the XSA and 17 from the CSC. Some of them have been observed with both telescopes; details of the observations are reviewed in the Appendix A. As shown in Figure 1, the source locations allow an analysis of the ISM along different lines of sight, and it also depicts the source position projected in the Galactic plane. The *XMM-Newton* spectra were reduced with the standard Scientific Analysis System (SAS) threads³ and the *Chandra* spectra with the standard CIAO threads⁴. We estimated the zero-order position for *Chandra* spectra with the *findzo* algorithm⁵. All spectra were rebinned to 25 counts per channel in order to use χ^2 statistics. The spectral fitting was performed with the *isis* data analysis package (Houck & Denicola 2000, version 1.6.2-30⁶).

3. Spectral fitting procedure

To estimate the O, Ne, and Fe column densities we carried out a broadband fit (11–24 Å) for each source listed in the Appendix A using a simple ISMabs*Bknpower model. The Bknpower component corresponds to a broken power law that in general provides a better fit to the continuum than a single unbroken power law. In the case of Sco X–1, we analyzed the spectra in the 15–24 Å region because of the absence of data below this wavelength range. The ISMabs model (Gatuzz et al. 2015) includes photoabsorption cross sections for neutrally, singly, and doubly ionized species, and the Fe photoabsorption cross-section is taken from metallic iron laboratory measurements (Kortright & Kim 2000). For each source all observations were fit simultaneously (i.e., using the same absorption parameters and varying the normalization for each observation); in the case of *Chandra*, we

¹ <http://xmm.esac.esa.int/xsa/>

² <http://cxc.harvard.edu/csc/>

³ <http://www.cosmos.esa.int/web/xmm-newton/sas-threads/>

⁴ <http://cxc.harvard.edu/ciao/threads/gspec.html>

⁵ <http://space.mit.edu/cxc/analysis/findzo/>

⁶ <http://space.mit.edu/asc/isis/>

Table 1. ISMabs column density values.

Source	ISMabs							
	$N(\text{H})$	$N(\text{O I})$	$N(\text{O II})$	$N(\text{O III})$	$N(\text{Ne I})$	$N(\text{Ne II})$	$N(\text{Ne III})$	$N(\text{Fe})$
4U 0614+091	9.3 ± 0.7	17.9 ± 2.3	< 0.57	–	4.6 ± 0.7	0.25 ± 0.17	< 0.02	0.49 ± 0.11
4U 0918–54	< 1.5	17.7 ± 1.7	< 0.01	< 0.2	2.3 ± 1.3	1.09 ± 1.04	< 0.01	0.72 ± 0.19
4U 1254–69	2.2 ± 0.2	14.6 ± 0.8	0.28 ± 0.24	0.34 ± 0.16	2.0 ± 0.3	0.79 ± 0.25	0.05 ± 0.04	0.59 ± 0.06
4U 1636–53	5.6 ± 1.7	22.9 ± 4.3	0.72 ± 0.32	0.35 ± 0.14	3.2 ± 0.9	0.78 ± 0.40	< 0.06	1.05 ± 0.22
4U 1728–16	6.6 ± 0.4	14.2 ± 1.2	0.30 ± 0.18	< 0.16	3.5 ± 0.4	0.54 ± 0.23	< 0.06	0.48 ± 0.06
4U 1735–44	3.2 ± 1.3	12.1 ± 1.7	0.53 ± 0.23	0.23 ± 0.10	2.9 ± 1.3	0.61 ± 0.42	< 0.16	0.76 ± 0.21
4U 1820–30	2.4 ± 0.8	8.9 ± 2.2	< 0.70	< 0.48	1.0 ± 0.7	0.16 ± 0.15	< 0.02	0.50 ± 0.15
4U 1915–05	4.7 ± 2.1	23.3 ± 4.3	< 0.02	–	4.4 ± 1.9	< 0.01	–	1.15 ± 0.48
4U 1957+11	3.4 ± 1.7	–	–	–	1.4 ± 1.6	< 0.16	< 0.01	0.67 ± 0.28
Aql X–1	3.6 ± 0.3	23.6 ± 1.2	< 0.06	0.21 ± 0.13	5.3 ± 0.3	0.58 ± 0.20	< 0.04	1.13 ± 0.07
Cygnus X–1	9.7 ± 0.4	21.4 ± 1.4	0.28 ± 0.18	0.47 ± 0.16	6.6 ± 0.3	0.39 ± 0.09	0.05 ± 0.02	0.98 ± 0.04
Cygnus X–2	4.3 ± 0.4	11.4 ± 0.8	0.45 ± 0.19	0.15 ± 0.08	2.6 ± 0.2	0.50 ± 0.10	0.06 ± 0.03	0.44 ± 0.05
EXO 0748–676	< 2.5	–	–	–	6.1 ± 2.8	–	–	–
GRO J1655–40	7.8 ± 0.3	26.2 ± 1.4	2.55 ± 1.08	3.37 ± 1.10	7.7 ± 0.3	1.11 ± 0.19	< 0.06	1.61 ± 0.13
GS 1826–238	3.1 ± 0.3	23.3 ± 1.5	0.28 ± 0.22	0.74 ± 0.25	5.0 ± 0.4	0.73 ± 0.28	< 0.01	1.07 ± 0.07
GX 339–4	4.1 ± 0.5	30.2 ± 3.1	< 1.79	< 1.19	4.9 ± 0.5	1.72 ± 0.36	0.19 ± 0.08	1.57 ± 0.17
GX 349+2	14.3 ± 3.3	–	–	–	11.0 ± 2.2	2.11 ± 1.54	< 0.20	2.31 ± 0.99
GX 9+9	7.4 ± 0.7	15.0 ± 1.7	0.36 ± 0.16	< 0.04	3.2 ± 0.4	0.60 ± 0.19	< 0.05	0.52 ± 0.09
J1753.5–0127	< 0.4	18.2 ± 1.4	< 0.22	0.53 ± 0.49	2.3 ± 0.8	< 0.15	< 0.06	0.53 ± 0.18
Swift J1808–3658	2.2 ± 1.3	7.0 ± 3.9	–	–	–	–	–	–
Swift J1910.2–0546	7.4 ± 1.2	12.9 ± 3.8	< 0.92	–	3.6 ± 0.6	0.42 ± 0.17	0.09 ± 0.04	0.91 ± 0.14
Sco X–1	2.1 ± 1.5	9.4 ± 1.4	< 0.11	< 0.01	–	–	–	0.42 ± 0.12
Ser X–1	3.0 ± 0.9	32.5 ± 3.0	< 1.08	0.52 ± 0.29	6.0 ± 0.7	1.04 ± 0.44	< 0.06	1.46 ± 0.21
XTE J1817–330	1.4 ± 0.4	11.1 ± 0.5	0.72 ± 0.24	0.34 ± 0.12	1.4 ± 0.2	0.41 ± 0.10	0.11 ± 0.04	0.46 ± 0.03

Notes. $N(\text{H})$ in units of 10^{21} cm^{-2} and metal column densities in units of 10^{17} cm^{-2} .

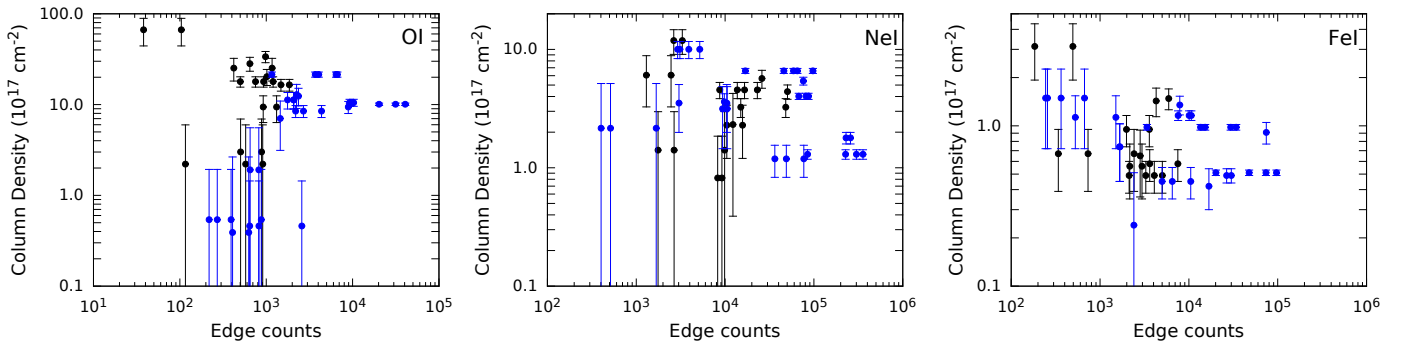


Fig. 2. ISMabs column densities for *Chandra* observations as a function of the number of counts. Black points correspond to *Chandra* TE-mode spectra and blue points to *Chandra* CC-mode spectra.

considered observations with timed-exposure (TE) readout mode and continuous clocking (CC) readout mode separately. The free parameters for the ISMabs fits were the H, O, Ne, and Fe column densities, including the O II, O III, Ne II, and Ne III ions.

Data statistics (e.g., number of counts in the wavelength region of interest) clearly have a significant impact on the absorption modeling. Figure 2 shows the ISMabs column densities obtained from the *Chandra* observations as a function of the number of counts in the O (21–24 Å), Ne (13–15 Å), and Fe (16–18 Å) absorption regions, which brings out a disparity in the O columns when the number of counts is low. This is probably because the details of the spatial distribution are lost in the CC read mode, and there is therefore no way to spatially separate the background from the source. This affects the spectra at long wavelengths where the effective area is smaller and where the background may become comparable to the source signal.

Specifically, CC-mode observations with less than approximately 2000 counts in the O K-edge region give rise to the outliers in the lefthand panel of Figure 2. Therefore, in the following procedures, we excluded observations with a limited number of counts in the O K-edge region (21–24 Å) and Ne K-edge region

(13–15 Å). Additional information on the influence of *Chandra* readout modes in high-resolution spectroscopy are given in Appendix B. Finally, for those sources with observations from both *Chandra* and *XMM-Newton*, we have found that the derived columns are in good agreement, so we take the average of the fit values.

4. Results and discussions

The fit results to all the observations in our sample are listed in Table 1. Upper limits for the column densities (i.e., the highest values obtained for each ion considering their upper errors) in units of 10^{17} cm^{-2} are $N(\text{O I}) < 32.46$; $N(\text{O II}) < 2.55$; $N(\text{O III}) < 3.37$; $N(\text{Ne I}) < 10.95$; $N(\text{Ne II}) < 2.11$; $N(\text{Ne III}) < 0.20$; and $N(\text{Fe}) < 2.31$. Figure 3 shows the column density distribution for each source. The hydrogen and neon column densities are mostly consistent and are homogeneously distributed along their average value; this is expected in neon since it does not form molecules. Oxygen and iron column densities, on the other hand, tend to be more dispersed along the different lines of sight. This is discussed further in Section 4.3.

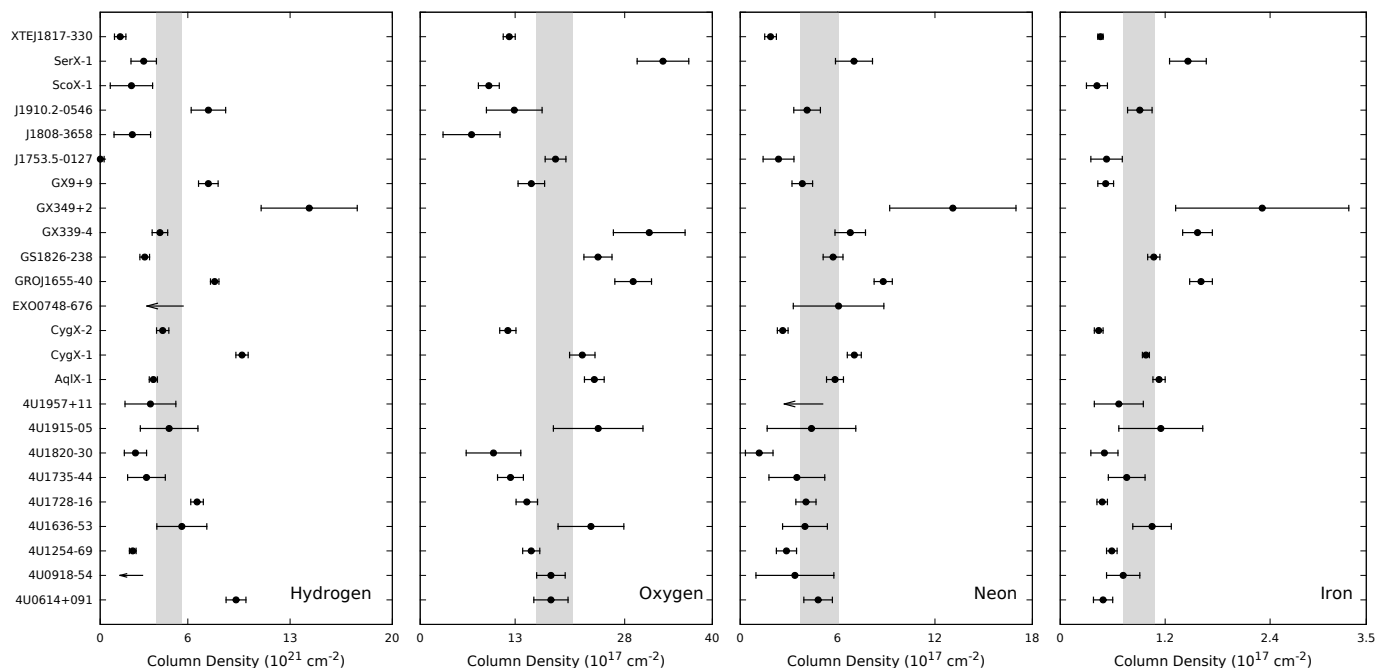


Fig. 3. ISMabs column densities values for each source. Gray boxes correspond to a 2σ region around the average value.

Table 2. Hydrogen column density comparison.

Source	$N(\text{H})$	21 cm survey ^a	21 cm survey ^b	21 cm survey ^c
4U 0614+091	9.30 ± 0.68	5.42	4.42	5.86
4U 0918-54	< 1.53	7.34	6.19	7.63
4U 1254-69	2.23 ± 0.23	2.85	2.15	3.46
4U 1636-53	5.59 ± 1.71	3.30	2.64	4.04
4U 1728-16	6.63 ± 0.43	2.10	1.98	3.31
4U 1735-44	3.17 ± 1.29	3.03	2.56	3.96
4U 1820-30	2.41 ± 0.76	1.52	1.32	2.33
4U 1915-05	4.72 ± 1.97	2.55	2.31	3.72
4U 1957+11	3.44 ± 1.74	1.31	1.23	2.01
Aql X-1	3.64 ± 0.28	3.28	2.86	4.30
Cygnus X-1	9.71 ± 0.42	8.10	7.81	9.25
Cygnus X-2	4.28 ± 0.42	2.20	1.88	3.09
EXO 0748-676	< 2.47	2.03	1.87	3.21
GRO J1655-40	7.84 ± 0.29	6.84	5.78	7.22
GS 1826-238	3.05 ± 0.33	1.83	1.68	3.00
GX 339-4	4.09 ± 0.53	5.00	3.74	5.18
GX 349+2	14.31 ± 3.29	6.12	4.69	6.13
GX 9+9	7.40 ± 0.67	2.10	1.98	3.31
J1753.5-0127	0.01 ± 0.26	1.64	1.66	2.98
Swift J1808-3658	2.20 ± 1.25	0.27	0.26	0.29
Swift J1910.2-0546	7.41 ± 1.18	2.24	2.44	2.24
Sco X-1	2.14 ± 1.45	1.47	1.40	2.54
Ser X-1	2.98 ± 0.87	4.43	3.98	5.42
XTE J1817-330	1.37 ± 0.39	1.58	1.39	2.29

Notes. $N(\text{H})$ in units of 10^{21} cm^{-2} . ^aDickey & Lockman (1990); ^bKalberla et al. (2005) and ^cWillingale et al. (2013).

4.1. Hydrogen column densities

A comparison of the ISMabs hydrogen column densities with the data sets from the 21 cm surveys (Dickey & Lockman 1990; Kalberla et al. 2005; Willingale et al. 2013) is provided in Table 2. The 21 cm hydrogen column densities correspond to the average value of all absorbers within 1° of the source position. It

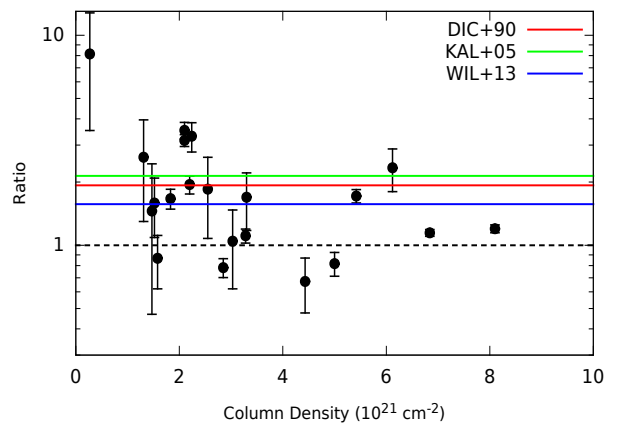


Fig. 4. Comparison of hydrogen column densities from different 21 cm surveys with the present ISMabs results. Black data points corresponds to the ISMabs/21 cm ratio using the Dickey & Lockman (1990) measurements. The solid color lines are linear fits to the ISMabs/21 cm values relative to the various determinations from the 21 cm surveys: Dickey & Lockman (1990, red line), Kalberla et al. (2005, green line), and Willingale et al. (2013, blue line).

is important to note that Dickey & Lockman (1990) and Kalberla et al. (2005) only consider the atomic H I column density, while Willingale et al. (2013) include both atomic and molecular hydrogen. Figure 4 shows a comparison of the 21 cm measurements with those derived from our ISMabs fits. Black data points correspond to the ISMabs/21 cm ratio using the Dickey & Lockman (1990) measurements. The solid color lines are linear fits to the ISMabs/21 cm values relative to the various determinations from the 21 cm surveys (Dickey & Lockman 1990; Kalberla et al. 2005; Willingale et al. 2013). For low column densities, the ISMabs values tend to be systematically higher than the 21 cm values, while for high column densities, the ISMabs values tend to be lower than the 21 cm values. We found overall that the

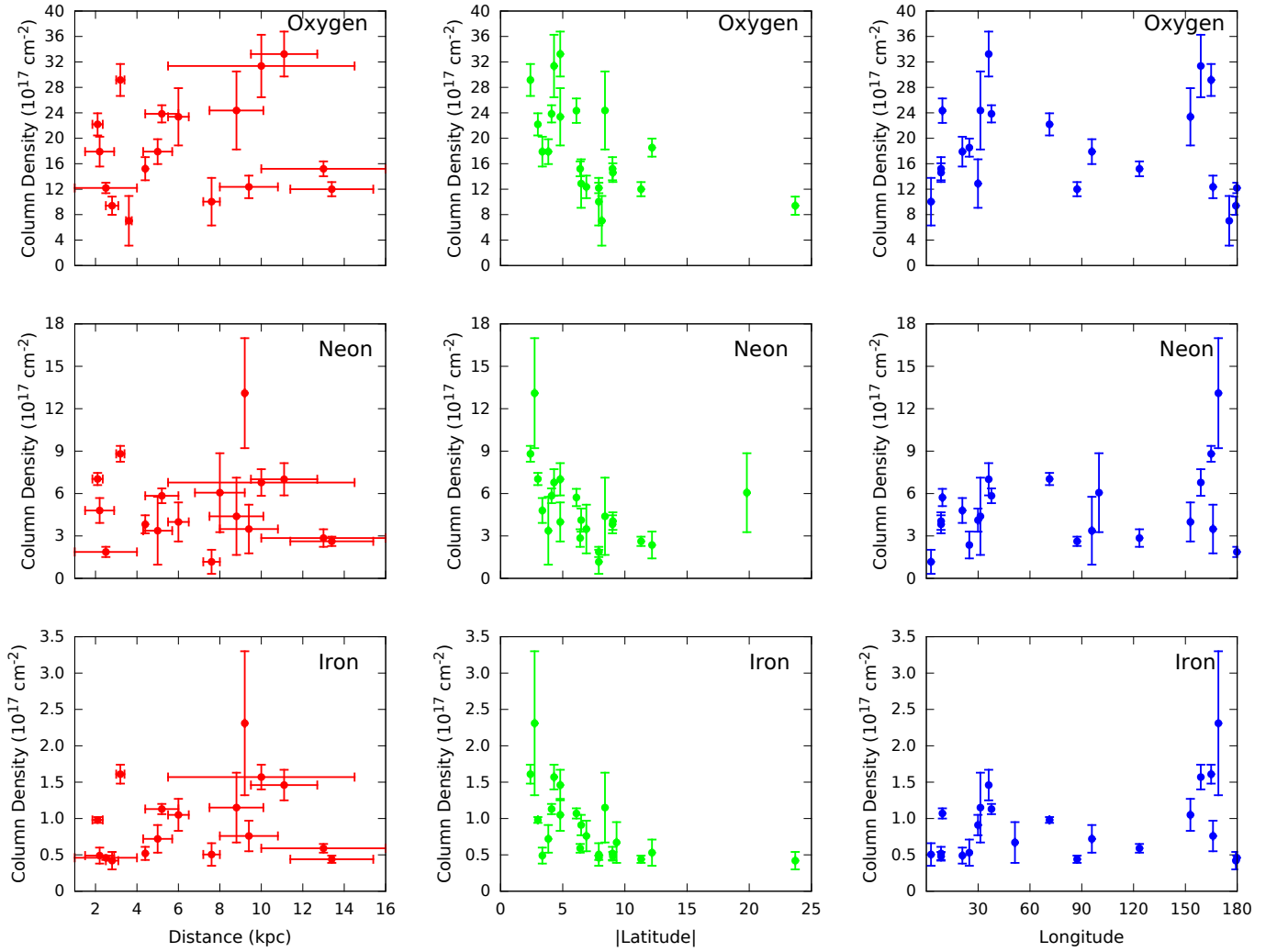


Fig. 5. Comparison of the oxygen, neon, and iron total column densities obtained from the ISMabs model as function of distance (left panels), latitude absolute value (middle panels), and longitude (right panels) for all the analyzed sources. Longitude has been rescaled to 0° – 180° .

best agreement of our results is with those from Willingale et al. (2013).

These discrepancies may arise from either a real difference in the intrinsic absorption or the continuum model; also, changes in the region around the X-ray source due to changes in the intrinsic column (e.g., the presence of winds) can increase absorption, and they are thus not resolved by the 21 cm surveys. These effects are more likely to be important in sources with strong stellar winds, such as Cyg X–1 and Sco X–1 (Gatuuz et al. 2014). On the other hand, the hydrogen column densities obtained from broadband fits are subject to the uncertainty of the assumed underlying continuum. In some cases, the characterization of the spectra with different models, such as *Powerlaw*, *Bknpower*, and *Blackbody*, leads to differences in the column densities despite similar statistics. Therefore, since we are not able to favor a continuum model based on fit statistics, we have adopted the *Bknpower* model for all observations for consistency and simplicity. We emphasize that the continuum model must be treated carefully in any attempt to perform an ISM analysis with X-ray high-resolution spectroscopy. In this respect our results are expected to be sensitive to the particular model used to describe the continuum in all sources.

4.2. ISM structure

Figure 5 shows a comparison of the oxygen, neon, and iron total column densities from the ISMabs model as a function of distance (left panels), latitude absolute value (central panels), and longitude (right panels) for all the analyzed sources. We have found that the column densities tend to increase with distance, because the slope is steeper in the case of oxygen, and the general trend is to decrease with galactic latitude. This behavior is expected because the ISM material density decreases in the vertical direction away from the Galactic plane. In the case of galactic longitude, it is difficult to establish a clear relationship with the column density but an increase at high longitude (i.e., away from the Galactic center) is hinted.

We have derived the column-density unweighted average considering all individual sources (in units of 10^{17} cm^{-2}): $N(\text{O}) = 18.43 \pm 2.53$, $N(\text{Ne}) = 4.91 \pm 1.19$, and $N(\text{Fe}) = 0.90 \pm 0.18$. Using the total column densities for each element, we estimated elemental abundances with the relation $N_x = A_x N_h$, where N_h is the hydrogen column density, A_x the abundance, and N_x the total column density of element x . The resulting values are listed in Table 3. The abundance behavior, on the other hand, tends to be constant with distance and latitude, and as for

Table 3. Abundance values.

Source	A_{O}	A_{Ne}	A_{Fe}
4U 0614+091	0.28 ± 0.06	0.43 ± 0.11	0.17 ± 0.05
4U 0918–54	< 1.73	< 1.84	< 1.49
4U 1254–69	1.01 ± 0.18	1.07 ± 0.34	0.84 ± 0.17
4U 1636–53	0.62 ± 0.31	0.60 ± 0.39	0.59 ± 0.31
4U 1728–16	0.33 ± 0.05	0.51 ± 0.11	0.23 ± 0.04
4U 1735–44	0.58 ± 0.32	0.92 ± 0.83	0.76 ± 0.52
4U 1820–30	0.61 ± 0.42	0.40 ± 0.42	0.66 ± 0.41
4U 1915–05	0.76 ± 0.51	0.78 ± 0.81	0.77 ± 0.64
4U 1957+11	–	< 0.38	0.62 ± 0.57
Aql X–1	0.97 ± 0.13	1.34 ± 0.22	0.98 ± 0.14
Cygnus X–1	0.34 ± 0.04	0.60 ± 0.06	0.32 ± 0.03
Cygnus X–2	0.41 ± 0.08	0.51 ± 0.11	0.33 ± 0.07
EXO 0748–676	–	< 2.04	–
GRO J1655–40	0.55 ± 0.07	0.94 ± 0.09	0.65 ± 0.08
GS 1826–238	1.18 ± 0.22	1.56 ± 0.34	1.11 ± 0.19
GX 339–4	1.13 ± 0.32	1.38 ± 0.37	1.21 ± 0.28
GX 349+2	–	0.76 ± 0.40	0.51 ± 0.34
GX 9+9	0.30 ± 0.06	0.43 ± 0.11	0.22 ± 0.06
J1753.5–0127	< 1.50	< 1.50	< 1.50
Swift J1808–3658	0.47 ± 0.53	–	–
Swift J1910.2–0546	0.26 ± 0.12	0.46 ± 0.17	0.39 ± 0.12
Sco X–1	0.65 ± 0.54	–	0.62 ± 0.60
Ser X–1	1.65 ± 0.66	1.96 ± 0.89	1.55 ± 0.67
XTE J1817–330	1.32 ± 0.46	1.13 ± 0.53	1.06 ± 0.37

Notes. Abundances are relative to the solar values of Grevesse & Sauval (1998).

longitude, sources with high hydrogen column densities tend to have increased abundances at low longitude values. Using the abundance values computed for all individual sources, we have derived unweighted average values relative to solar (Grevesse & Sauval 1998) of $A_{\text{O}} = 0.70 \pm 0.26$, $A_{\text{Ne}} = 0.87 \pm 0.35$, and $A_{\text{Fe}} = 0.67 \pm 0.28$.

The comparison of the oxygen and iron total column densities as a function of the neon column density is shown in Figure 6, including contributions from the neutrally, singly, and doubly ionized species for each element. The best-fit $N_{\text{x}}/N_{\text{Ne}}$ abundance ratio for all sources is plotted with the solid red line; ratios from Grevesse & Sauval (1998), Asplund et al. (2009), Lodders et al. (2009) and Juett et al. (2004) are also shown. As a noble gas, neon is a suitable baseline since it is only found in atomic form. We find an average ratio of $N(\text{O})/N(\text{Ne}) = 4.16 \pm 0.22$, which is greater than the estimate by Juett et al. (2006) of 3.7 ± 0.3 and lower than the solar values of 4.79 (Lodders et al. 2009), 5.36 (Grevesse & Sauval 1998), and 5.75 (Asplund et al. 2009). We also obtain an average ratio of $N(\text{Fe})/N(\text{Ne}) = 0.18 \pm 0.01$, in relatively close agreement with Juett et al. (2006) (0.15 ± 0.01) and lower than the solar ratios by Grevesse & Sauval (1998), Lodders et al. (2009), and Asplund et al. (2009) of 0.26, 0.25, and 0.37, respectively.

The presence of ionized species in the ISM is not negligible and must be considered in order to perform a reliable chemical analysis of its environment. Figure 7 shows a comparison of the O II/O I , O III/O I , Ne II/Ne I , and Ne III/Ne I ionization fractions as a function of distance, latitude absolute value, and longitude. Unlike the column densities, the ionization fractions tend to be approximately constant with the geometric parameters. This result agrees with previous findings regarding the dominance of the ISM cold phase characterized by a low ionization degree (Gatuzz et al. 2013a,b, 2014, 2015). We obtained the following average values: $\text{O II/O I} = 0.03 \pm 0.01$, $\text{O III/O I} = 0.03 \pm 0.02$, $\text{Ne II/Ne I} = 0.21 \pm 0.05$, and $\text{Ne III/Ne I} = 0.03 \pm 0.02$.

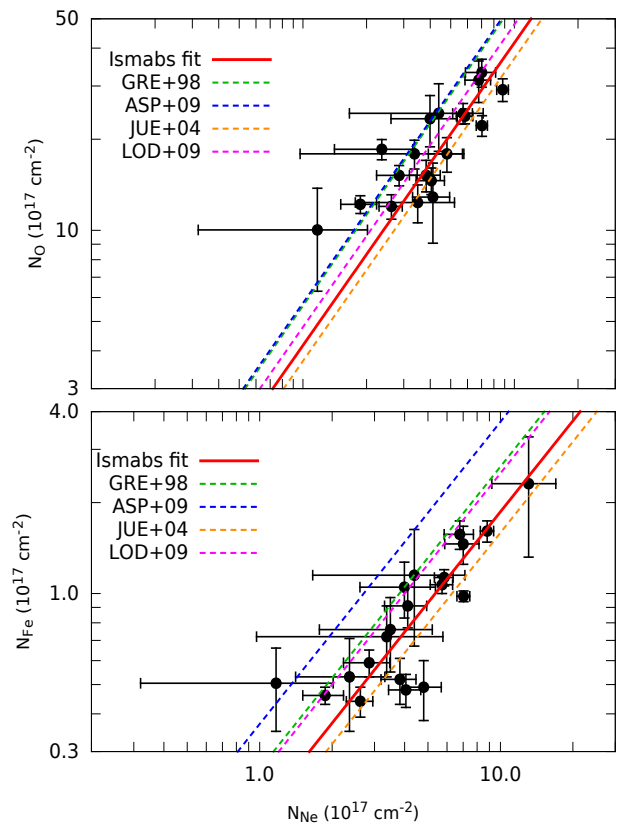


Fig. 6. Comparison of the abundance ratios $N_{\text{O}}/N_{\text{Ne}}$ (top panel) and $N_{\text{Fe}}/N_{\text{Ne}}$ (bottom panel) obtained from the broadband fit with ISMabs for all the analyzed sources. The best-fit $N_{\text{x}}/N_{\text{Ne}}$ ratio for all sources is plotted with a solid red line. Ratios obtained from Grevesse & Sauval (1998), Asplund et al. (2009), Lodders et al. (2009), and Juett et al. (2004) are respectively shown with green, blue, orange, and magenta dashed lines.

4.3. Molecular absorption features

The search for molecular and dust spectral signatures is a topic of current interest in ISM astrophysics. Lee et al. (2009) argue that *Chandra* and *XMM-Newton* high-resolution spectra provide a resource for constraining dust properties (e.g., distribution, composition, and abundances). Absorption features due to molecules and dust have been studied previously using LMXB (de Vries & Costantini 2009; Kaastra et al. 2009; Pinto et al. 2010; Costantini et al. 2012; Pinto et al. 2013); in particular, de Vries & Costantini (2009) estimate an oxygen depletion rate to the solid state of 30–50% from an *XMM-Newton* RGS spectrum of Sco X–1. However, García et al. (2011) show that, by taking an improved photoabsorption cross section into account for atomic oxygen, which itself takes Auger damping into account, the same observation could be adequately modeled without invoking molecular or dust contributions. The best X-ray absorption model should include both atomic and molecular cross sections. However, since the spectral features from solid compounds are expected to be weak, an accurate modeling of the atomic components is a prerequisite.

In this respect, Pinto et al. (2010) previously analyzed the *XMM-Newton* spectra of the binary GS 1826–238, and after modeling the atomic component, they included molecular and dust contributions to diminish the high residuals near the oxygen edge. They derived column densities for andradite ($\text{Ca}_3\text{Fe}_2\text{Si}_3\text{O}_{12}$), amorphous ice (H_2O), carbon monoxide (CO),

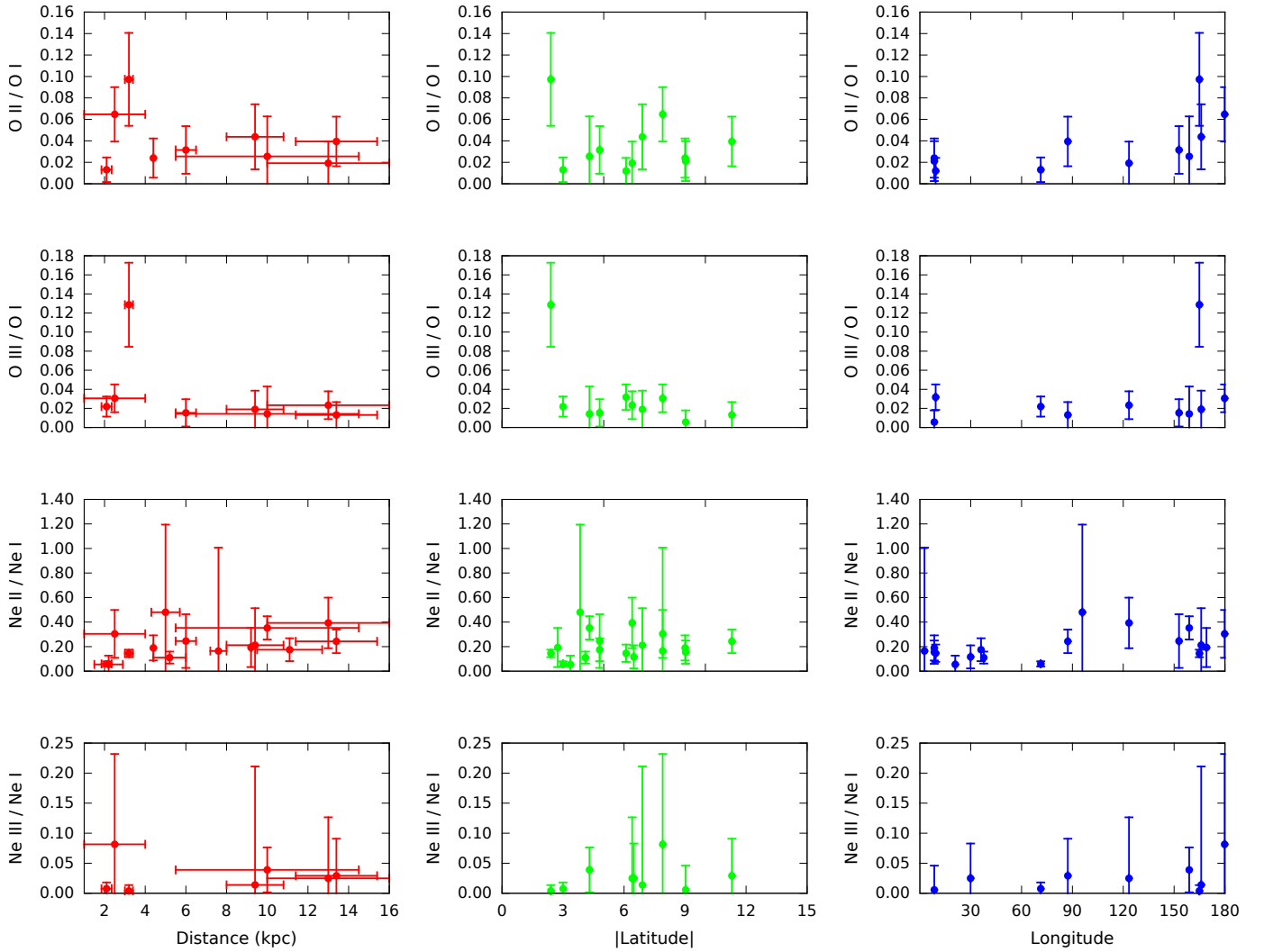


Fig. 7. Comparison of the ionization fractions $O\ II/O\ I$, $O\ III/O\ I$, $Ne\ II/Ne\ I$, and $Ne\ III/Ne\ I$ obtained with the ISMabs model as a function of distance (left panels), the latitude absolute value (middle panels), and longitude (right panels) for all these sources. Longitude has been rescaled to 0° – 180° .

and hercynite ($FeAl_2O_4$); however, their model included the same undamped atomic cross sections as used in previous studies. Figure 8 shows *XMM-Newton* spectra of GS 1826–238 in the 21–24 Å region modeled by ISMabs, which considers a more recent and Auger-damped atomic cross section.

Although ISMabs includes neither molecular nor solid photoabsorption cross-sections, it leads to a good fit of the O K-edge absorption features with well-distributed small residuals; that is, the apparent lack of absorption previously perceived by Pinto et al. (2010) was due, in our opinion, to a poor atomic model. Our results imply an upper limit to the amount of oxygen that can be in a molecular or a solid form. A quantitative estimate for this limit requires simultaneous fits using both our accurate atomic oxygen K shell cross-sections and the best available models for absorption by molecules and dust. This will be the subject of future investigations.

It is important to note that, since the valence electronic levels of molecules or dust are more fully occupied than those of atoms, the $K\alpha$ resonance lines from molecules and dust will in general be weaker than atoms, or absent. Thus, the addition of molecules or dust to an atomic model when fitting to observed ISM X-ray spectra will lead to a higher ratio of edge to line. Our fits do not

show a systematic discrepancy or statistically significant errors in this ratio, thus reinforcing the conclusion that molecules and grains are a minor contributor to the absorption in the spectral region near the oxygen K edge.

5. Conclusions

We performed a thorough analysis of the ISM along 24 lines of sight by means of high-resolution X-ray spectroscopy with spectra obtained from the *Chandra* and *XMM-Newton* space observatories. This is the most complete study to date of this type, and it considered O and Ne charge states. We found that data statistics (i.e., number of counts for a given wavelength region) has a sizeable impact on the analysis, which is particularly important in the case of *Chandra* observations taken in CC mode because they require a higher number of counts than those in TE mode in order to avoid background contamination. For sources observed with both telescopes, the derived column densities are in good agreement, so average values are listed.

Using the ISMabs X-ray absorption model, we obtained upper limits for the column densities of H I, O I, O II, O III, Ne I, Ne II, Ne III, and metallic Fe. In the case of hydrogen, we found differences between our fits and the 21 cm surveys. These dis-

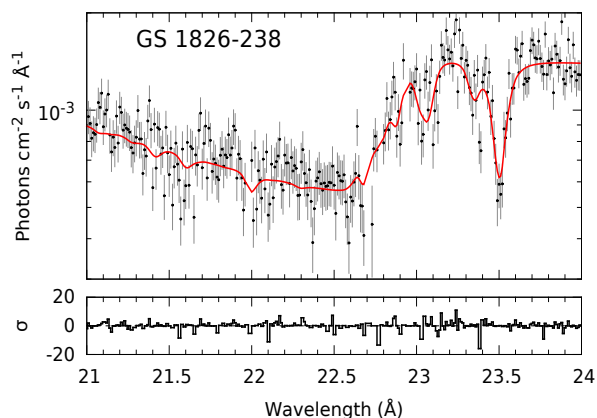


Fig. 8. GS 1826–238 *XMM-Newton* spectra in the oxygen K-edge region. Observations were combined for illustrative purposes.

crepancies may arise from intrinsic absorption variabilities in each source, as well as from the particular choice of continuum representation. Our measurements indicate an increase in the column densities with source distance and a decrease with galactic latitude. We find that the ionization fractions, on the contrary, tend to be constant with distance and latitude reinforcing previous conclusions regarding the dominance of the neutral ISM component.

We also derived the $N(\text{O})/N(\text{Ne})$ and $N(\text{Fe})/N(\text{Ne})$ abundance ratios finding lower values than solar (Grevesse & Sauval 1998). Using the total column densities, we estimated the O, Ne, and Fe abundances to be $\sim 70\%$, $\sim 87\%$, and $\sim 67\%$, respectively, relative to the solar standards of Grevesse & Sauval (1998) and $\sim 97\%$, $\sim 122\%$, and Fe $\sim 67\%$ relative to the revised values of Asplund et al. (2009). In general, the abundances show a different trend to the one observed in the column densities: they tend to be constant with distance and latitude.

It is important to note that this study only considers a small fraction of the local ISM environment because of the lack of a larger database of bright LMXB to perform a more extensive analysis. Observations with new-generation instrumentation such as *Astro-H* will allow a finer examination of the ISM large structures. The present work will be followed by a search and study of molecular and dust absorption features.

Appendix A: Data sample

For this analysis we used a sample of 84 observations, and the details of the *Chandra* and *XMM-Newton* observations are listed in Tables A.1–A.2. The number of counts for each observation in the broadband fit region (11–24 Å), O K-edge region (21–24 Å), Ne K-edge region (13–15 Å), and Fe L-edge region (16–18 Å) are also included. In the case of *Chandra*, 20 and 29 observations were taken in TE-mode and CC-mode, respectively.

Figures A.1–A.2 show the best broadband fit for each source in flux units. In cases where more than one observation is present, the observations are fit simultaneously, and they vary the continuum parameters so have only been combined for illustrative purposes. The best-fit model is indicated by a solid red line. In the case of Sco X-1, the broadband fit was performed in the 15–24 Å wavelength range owing to the absence of data below 15 Å (see Figure A.3). The dominant observed absorption features correspond to the O K edge (~ 23 Å), Ne K edge (~ 14 Å),

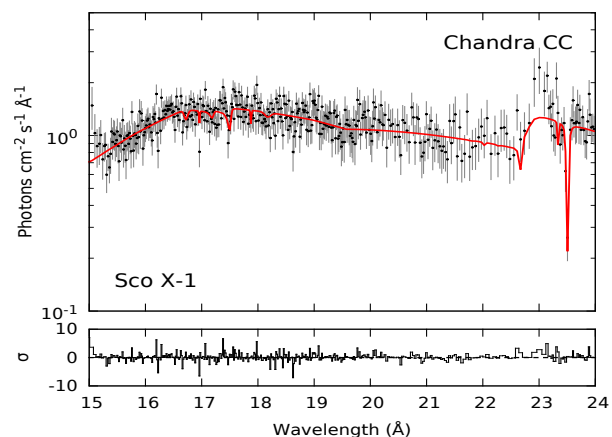


Fig. A.3. ISMabs best broadband fits for Sco X-1. Observations were combined for illustrative purposes.

Fe L edge (~ 17 Å), and the $\text{O I K}\alpha$ transition (~ 23.5 Å). In general, a smooth residual distribution (bottom panels) around these edges is observed, indicating modeling accuracy that relies on the latest atomic data. It must be emphasized that the absence of molecular photoabsorption cross-sections in the ISMabs model (except for metallic Fe) does not represent a spectral fitting limitation. This is discussed in Sect. 4.3. All data were rebinned to 25 counts per channel and combined for illustrative purposes

Appendix B: *Chandra* CC-mode notes

The *Chandra* CC-mode provides a fast readout mode to decrease the pileup effect in bright sources: i.e., the detection of two photons as a single event with the sum of their energies. While in TE-mode the events are collected for a specific time frame and then read out collectively, in CC-mode they are read out continuously by collapsing them to one row. In the case of a low-count regime, CC-mode data must be analyzed carefully because they can be affected by the background that cannot be separated from the source spectrum.

As an example of this effect, we show a comparison in Figure B.1 of the 4U 1636–53 spectra in the 11–24 Å region as obtained by the *Chandra* TE-mode, CC-mode, and *XMM-Newton*. All data have been rebinned to 25 counts per channel and combined for illustrative purposes. The total number of counts in the oxygen absorption region (21–24 Å) without rebinning is 1591 (CC-mode), 1035 (TE-mode), and 28240 (RGS). The O I and $\text{O II K}\alpha$ absorption lines at ~ 23.5 Å and ~ 23.35 Å, respectively, are clearly observed in the TE-mode and the RGS data, but they cannot be detected in CC-mode due to background contamination that becomes dominant at ~ 18 – 20 Å. For this reason and based on previous tests, we discarded from our analyses the oxygen column densities derived from observations in CC mode with fewer than 2000 counts in the oxygen K-shell region.

References

- Asplund, M., Grevesse, N., Sauval, A. J., & Scott, P. 2009, *ARA&A*, 47, 481
 Buote, D. A., Zappacosta, L., Fang, T., et al. 2009, *ApJ*, 695, 1351
 Costantini, E., Pinto, C., Kaastra, J. S., et al. 2012, *A&A*, 539, A32
 de Vries, C. P. & Costantini, E. 2009, *A&A*, 497, 393
 Dickey, J. M. & Lockman, F. J. 1990, *ARA&A*, 28, 215
 Fang, T., Buote, D. A., Humphrey, P. J., et al. 2010, *ApJ*, 714, 1715
 Galloway, D. K., Munro, M. P., Hartman, J. M., Psaltis, D., & Chakrabarty, D. 2008, *ApJS*, 179, 360

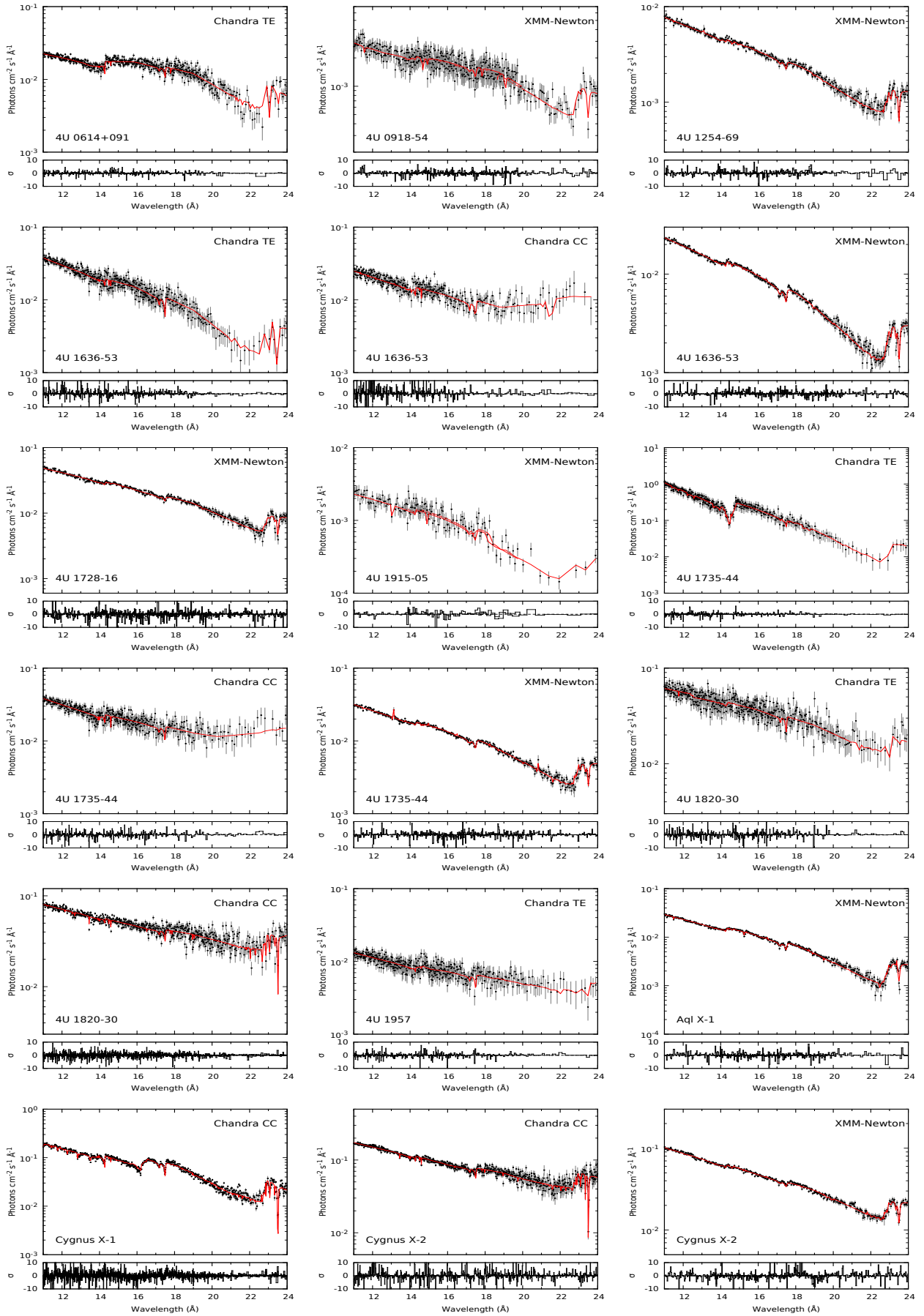


Fig. A.1. ISMabs best broadband fits for the analyzed sources where observations are combined for illustrative purposes. In the case of *Chandra* the read mode (CC-mode or TE-mode) is indicated.

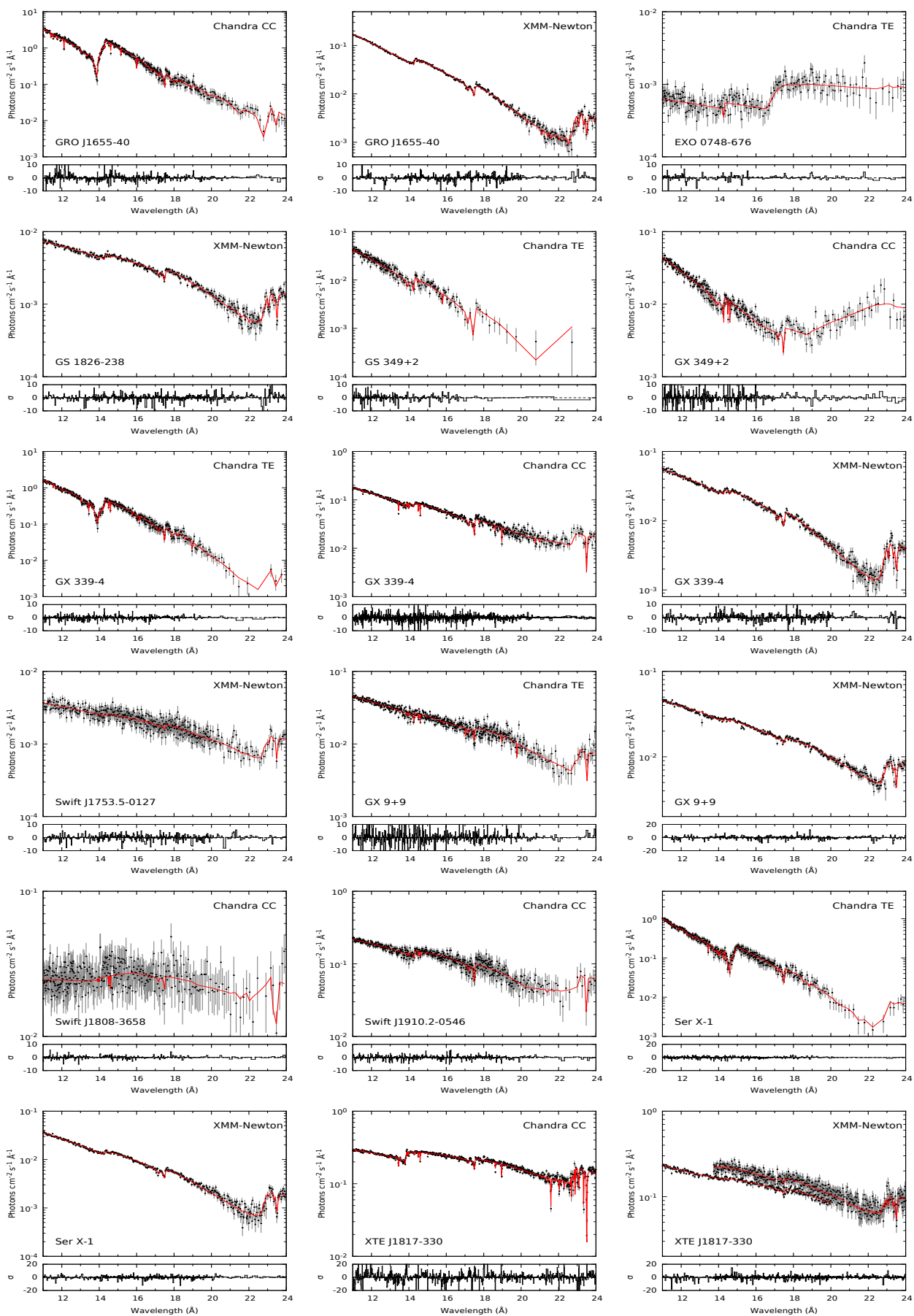


Fig. A.2. ISMabs best broadband fits for the analyzed sources where observations are combined for illustrative purposes. In the case of *Chandra*, the read mode (CC-mode or TE-mode) is indicated.

Table A.1. *Chandra* observation list.

Source	Galactic coordinates	Distance (kpc)	ObsID	Mode	Counts			
					11–24 Å	O-edge	Ne-edge	Fe-edge
4U 0614+091	(200.87, −3.36)	2.2 ± 0.7^a	10759	TE	233091	932	16561	4084
			10760	TE	191848	752	13715	3275
			10857	TE	346327	1201	23081	5024
			10858	TE	121262	501	8698	2126
4U 1636–53	(332.9, −4.8)	6.0 ± 0.5^b	105	TE	244922	1170	15732	3589
			1939	TE	212637	421	10453	1984
			6635	CC	52613	408	3026	527
			6636	CC	209101	627	10455	1507
4U 1735–44	(346.0, −6.9)	9.4 ± 1.4^c	704	TE	196485	1018	12263	2828
			6637	CC	192055	651	10555	1673
			6638	CC	184711	821	9370	1658
4U 1820–30	(2.7, −7.9)	7.6 ± 0.4^d	1021	TE	113582	923	8252	2160
			1022	TE	108264	1318	9216	2966
			6633	CC	383259	2189	36282	4991
			6634	CC	516960	2699	48878	6502
4U 1957+11	(51.30, −9.33)	–	7032	CC	814603	4367	76919	10493
			4552	TE	168011	911	9882	2415
			10659	TE	29828	116	1759	339
			10660	TE	36181	578	2666	732
Cygnus X–1	(71.3, 3.0)	2.10 ± 0.25^e	1511	CC	247819	1161	16914	3370
			2415	CC	890793	3692	58878	13539
			3407	CC	1164551	6437	65150	29544
			3724	CC	987399	6665	45801	34115
Cygnus X–2	(87.3, −11.3)	13.4 ± 2.0^c	3815	CC	1501955	4054	97369	15254
			8170	CC	2156452	10280	257811	30039
			8599	CC	2010493	9237	229962	26597
EXO 0748–676	(279.97, −19.81)	8.0 ± 1.2^c	4573	TE	29582	883	2464	1235
GRO J1655–40	(344.98, 2.45)	3.2 ± 0.2^c	4574	TE	16736	505	1300	681
			5461	CC	1345632	2364	75958	7893
GX 339–4	(338.93, −4.32)	10.0 ± 4.5^f	4420	TE	928061	647	50413	5925
			4569	CC	1534889	1766	67573	7565
			4570	CC	1561121	2077	81294	10068
			4571	CC	1559603	2084	86894	10657
GX 349+2	(349.10, 2.74)	9.2^g	715	TE	96903	38	2643	184
			3354	TE	153152	104	3300	494
			6628	CC	152618	271	3098	256
			7336	CC	138413	218	2922	244
			12199	CC	210418	392	3904	364
			13221	CC	179170	876	5184	668
GX 9+9	(8.5, 9.0)	4.4^g	703	TE	226157	1481	15013	3626
			11072	TE	831449	1853	48170	7514
Sco X–1	(359, 23.7)	2.8 ± 0.3^c	3505	CC	63953	8914	232	16798
Ser X–1	(36.11, 4.84)	11.1 ± 1.6^c	700	TE	588628	981	25989	4283
Swift J1808–3658	(355.38, −8.14)	3.61 ± 0.14^c	6297	CC	82782	1454	8500	2404
Swift J1910.2–0546	(29.90, −06.84)	–	14634	CC	1218802	2246	9806	74359
XTE J1817–330	(359.8, −7.9)	2.5 ± 1.5^h	6615	CC	2622175	40674	356751	96856
			6616	CC	2790705	31440	300764	73725
			6617	CC	2889136	20257	227411	47640
			6618	CC	930503	9296	84865	20114

Notes. Distances taken from: ^aPaerels et al. (2001); ^bGalloway et al. (2008); ^cJonker & Nelemans (2004); ^dKuulkers et al. (2003); ^eZiōłkowski (2005); ^fHynes et al. (2004); ^gGrimm et al. (2002); and ^hSala & Greiner (2006).

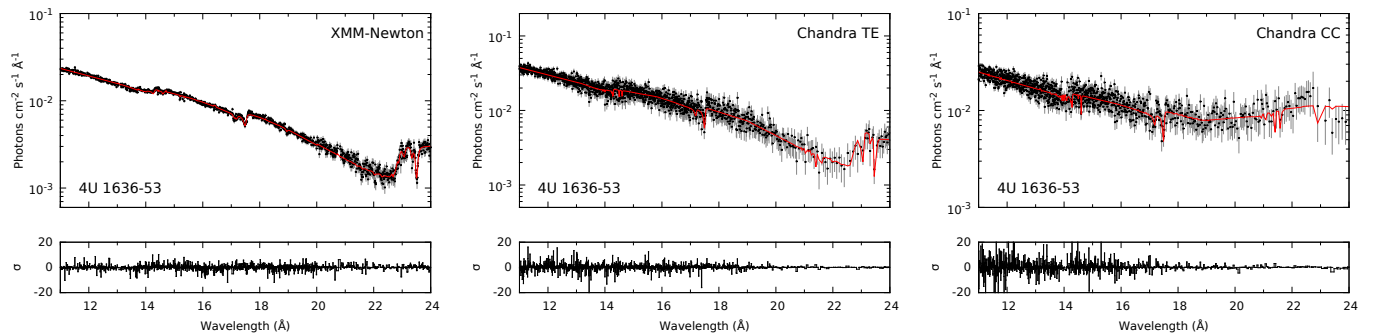


Fig. B.1. Comparison of the 4U 1636–53 spectra obtained with *XMM-Newton*, *Chandra* TE-mode, and *Chandra* CC-mode in the broadband region. Observations are combined for illustrative purposes.

Table A.2. *XMM-Newton* observation list.

Source	Galactic coordinates	Distance (kpc)	ObsID	Counts			
				11–24 Å	O-edge	Ne-edge	Fe-edge
4U 0918–54	(275.85, –3.84)	5.0 ± 0.7^a	0061140101	63368	3194	15290	13279
4U 1254–69	(303.4, –6.4)	13.0 ± 3.0^b	0060740101	50859	1862	13606	9325
			0060740901	87761	3387	23365	16126
			0405510301	205907	6954	55922	37401
			0405510401	195814	6879	53484	34759
4U 1636–53	(332.9, –4.8)	6.0 ± 0.5^c	0405510501	193851	6796	52792	34008
			0500350301	253139	6259	71945	43865
			0500350401	361332	8840	102801	62238
			0606070101	219009	5326	62231	37616
4U 1728–16	(8.5, 9.03)	4.4^d	0606070301	333832	7815	95606	57434
			0090340101	233545	9139	62514	42769
4U 1735–44	(346.0, –6.9)	9.4 ± 1.4^a	0090340601	469351	18294	125676	86571
			0090340201	334452	10617	91311	59523
4U 1915–05 Aql X–1	(31.3, –8.4) (37.7, –4.1)	8.8 ± 1.3^a 5.2 ± 0.8^a	0693490201	902050	26482	245610	160800
			0085290301	14733	404	4324	2680
Cygnus X–2	(87.3, –11.3)	13.4 ± 2.0^a	0303220301	114415	2652	31899	19293
			0303220401	128025	2971	35380	22738
			0406700201	688187	12644	199459	113576
			0111360101	587885	28796	151920	113464
GRO J1655–40	(344.9, 2.4)	3.2 ± 0.2^a	0303280101	1333661	55636	342757	249293
			0112921401	475112	3326	138554	52879
			0112921501	482485	3266	139218	52801
GS 1826–238	(9.3, –6.1)	6.7^c	0112921601	516085	3608	149411	57451
			0150390101	345896	10758	94316	65058
GX 339–4	(338.9, –4.3)	10.0 ± 4.5^e	0150390301	304791	9413	82648	57744
			0148220201	337152	5453	98860	54234
GX 9+9	(8.5, 9.0)	4.4^d	0148220301	259545	4072	76761	40983
			0090340101	233545	9139	62514	42769
			0090340601	469351	18294	125676	86571
			0694860301	665729	22912	180651	121842
Ser X–1	(36.1, 4.8)	11.1 ± 1.6^a	0084020401	209100	2904	60939	30021
			0084020501	199357	2713	58235	28839
			0084020601	206092	2778	60447	29665
			0311590901	833709	3987	21190	16690
J1753.5–0127	(24.89, 12.18)	–	0311590501	1099719	20490	275954	202834
XTE J1817–330	(359.8, –7.9)	2.5 ± 1.5^f					

Notes. Distances from ^aJonker & Nelemans (2004); ^bin't Zand et al. (2003); ^cGalloway et al. (2008); ^dGrimm et al. (2002); ^eHynes et al. (2004); and ^fSala & Greiner (2006).

- García, J., Mendoza, C., Bautista, M. A., et al. 2005, *ApJS*, 158, 68
García, J., Ramírez, J. M., Kallman, T. R., et al. 2011, *ApJ*, 731, L15
Gatuzz, E., García, J., Kallman, T. R., Mendoza, C., & Gorczyca, T. W. 2015, *ApJ*, 800, 29
Gatuzz, E., García, J., Mendoza, C., et al. 2014, *ApJ*, 790, 131
Gatuzz, E., García, J., Mendoza, C., et al. 2013a, *ApJ*, 778, 83
Gatuzz, E., García, J., Mendoza, C., et al. 2013b, *ApJ*, 768, 60
Gorczyca, T. W., Bautista, M. A., Hasoglu, M. F., et al. 2013, *ApJ*, 779, 78
Gorczyca, T. W. & McLaughlin, B. M. 2000, *J. Phys. B: At. Mol. Opt. Phys.*, 33, L859
Grevesse, N. & Sauval, A. J. 1998, *Space Sci. Rev.*, 85, 161
Grimm, H.-J., Gilfanov, M., & Sunyaev, R. 2002, *A&A*, 391, 923
Houck, J. C. & Denicola, L. A. 2000, in *Astronomical Society of the Pacific Conference Series*, Vol. 216, *Astronomical Data Analysis Software and Systems IX*, ed. N. Manset, C. Veillet, & D. Crabtree, 591
Hynes, R. I., Steeghs, D., Casares, J., Charles, P. A., & O'Brien, K. 2004, *ApJ*, 609, 317
in't Zand, J. J. M., Kuulkers, E., Verbunt, F., Heise, J., & Cornelisse, R. 2003, *A&A*, 411, L487
Jonker, P. G. & Nelemans, G. 2004, *MNRAS*, 354, 355
Juett, A. M., Schulz, N. S., & Chakrabarty, D. 2004, *ApJ*, 612, 308
Juett, A. M., Schulz, N. S., Chakrabarty, D., & Gorczyca, T. W. 2006, *ApJ*, 648, 1066
Kaastra, J. S., de Vries, C. P., Costantini, E., & den Herder, J. W. A. 2009, *A&A*, 497, 291
Kalberla, P. M. W., Burton, W. B., Hartmann, D., et al. 2005, *A&A*, 440, 775
Kortright, J. B. & Kim, S.-K. 2000, *Phys. Rev. B*, 62, 12216
Kuulkers, E., den Hartog, P. R., in't Zand, J. J. M., et al. 2003, *A&A*, 399, 663
Lee, J. C., Xiang, J., Ravel, B., Kortright, J., & Flanagan, K. 2009, *ApJ*, 702, 970
Liao, J.-Y., Zhang, S.-N., & Yao, Y. 2013, *ApJ*, 774, 116
Lodders, K., Palme, H., & Gail, H.-P. 2009, *Landolt Börnstein* [arXiv:0901.1149]
Luo, Y. & Fang, T. 2014, *ApJ*, 780, 170
Nicastrò, F. 2014, in *The X-ray Universe 2014*, 11
Paelers, F., Brinkman, A. C., van der Meer, R. L. J., et al. 2001, *ApJ*, 546, 338
Pinto, C., Kaastra, J. S., Costantini, E., & de Vries, C. 2013, *A&A*, 551, A25
Pinto, C., Kaastra, J. S., Costantini, E., & Verbunt, F. 2010, *A&A*, 521, A79
Ren, B., Fang, T., & Buote, D. A. 2014, *ApJ*, 782, L6
Sala, G. & Greiner, J. 2006, *The Astronomer's Telegram*, 791, 1
Schulz, N. S., Cui, W., Canizares, C. R., et al. 2002, *ApJ*, 565, 1141
Takei, Y., Fujimoto, R., Mitsuda, K., & Onaka, T. 2002, *ApJ*, 581, 307
Willingale, R., Starling, R. L. C., Beardmore, A. P., Tanvir, N. R., & O'Brien, P. T. 2013, *MNRAS*, 431, 394
Yao, Y., Schulz, N. S., Gu, M. F., Nowak, M. A., & Canizares, C. R. 2009, *ApJ*, 696, 1418
Ziótkowski, J. 2005, *MNRAS*, 358, 851